

A Novel Fiber Bragg Grating Three-Dimensional Force Sensor for Medical Robotics

Qiaokang Liang , Senior Member, IEEE, Songtao Ouyang , Jianyong Long , Member, IEEE,
Li Zhou , and Dan Zhang , Senior Member, IEEE

Abstract—This article introduces a novel Fiber Bragg Grating (FBG) 3-D force sensor designed for the end-effectors of medical robots. The sensor incorporates a specially designed layered elastic structure, achieving miniaturization, structural self-decoupling, and high-sensitivity 3-D force measurement through a cleverly compact spatial design and a reasoned layout of 5 FBGs. The construction of the theoretical model successfully decouples temperature and force. Simulation experiments determine the sensor's operational frequency range to be 0–403.6 Hz, validated through rapid prototype verification using 3-D printing technology. Static experiments reveal that the sensor's maximum measurement range and minimum resolution are ± 5 N and 4.95 mN, respectively. The maximum sensitivity and minimum interaxis coupling are determined to be 201.86 pm/N, 0.01%F.S.(F_y–F_z), respectively. In dynamic experiments, the minimum tracking error is 3.89% F.S and successfully adapts to the end-effector of a robotic arm. Remarkably, the sensor excels in force detection during medical palpation and acupuncture procedures, validating its effectiveness and practicality in real-world applications. This study presents a reliable and high-performance end-effector force-sensing solution for the field of medical robotics.

Index Terms—Fiber Bragg Grating (FBG), medical robots, structure self-decoupling, three-dimensional (3-D) force sensor.

I. INTRODUCTION

WITH the widespread application of robots in surgical procedures, sensing technology becomes more

Manuscript received 5 April 2024; accepted 27 May 2024. Recommended by Technical Editor Joshua A Schultz and Senior Editor Jun Ueda. This work was supported in part by the Project of the National Key Research and Development Program of China under Grant 2022YFB4703103, and in part by the National Natural Science Foundation of China under Grant 62303175 and Grant 62073129. (Corresponding author: Jianyong Long.)

Qiaokang Liang, Songtao Ouyang, Jianyong Long, and Li Zhou are with the National Engineering Research Center for Robot Vision Perception and Control, College of Electrical and Information Engineering, Hunan University, Changsha 410082, China (e-mail: qiaokang@hnu.edu.cn; songtao@hnu.edu.cn; lji_cv@hnu.edu.cn; tda2030@hnu.edu.cn).

Dan Zhang is with the Department of Mechanical Engineering, The Hong Kong Polytechnic University 100872, Hong Kong (e-mail: dan.zhang@polyu.edu.hk).

Color versions of one or more figures in this article are available at <https://doi.org/10.1109/TMECH.2024.3408427>.

Digital Object Identifier 10.1109/TMECH.2024.3408427

important [1]. Force sensing technology, as a critical constituent of robotic technology, centers around force sensors. During surgery, the robotic end-effector can, by configuring high-precision multidimensional force sensors, engage in force perception feedback and control, thereby reducing the risks of tissue damage or bleeding that may arise due to insufficient force transmission capabilities [2], [3]. Therefore, it is a challenging and significant task to design a high-performance multidimensional force sensor with the characteristics of miniaturization, high sensitivity, low coupling, antielectromagnetic interference, and biocompatibility.

The solution of low coupling of force sensors can be divided into structural self-decoupling and algorithm decoupling. Compared with algorithm decoupling, structural self-decoupling can eliminate coupling in essence, but it is more challenging [4]. Currently, the structural design of robot force sensors can be categorized into various types such as the cross-beam [5], E-shaped [6], columnar [7], [8], and L-shaped [9] configurations. To further enhance the sensitivity and reduce coupling, many scholars and researchers have proposed new optimized structures [10], [11], [12], [13]. While their work was commendable, it relied on electromagnetic-sensitive components, which come with several drawbacks, including complex structural wiring, susceptibility to electromagnetic interference and environmental humidity effects, significant nonlinear errors, and zero-temperature shift. Consequently, these limitations hinder the application of such sensors in medical robots.

In recent years, Fiber Bragg Grating (FBG) has found extensive application in the field of force sensing for medical robots, owing to its advantages such as electromagnetic interference resistance, compact size, lightweight, and excellent biocompatibility [14], [15]. Lai et al. [16] proposed a torque sensor suitable for minimally invasive surgery (MIS) based on FBG, achieving miniaturization and high sensitivity (0.062 N · mm). However, the consideration of multidimensional force measurement and structural decoupling was absent. Xiong et al. [17] designed a 3-D force sensor for robot foot soles using a cross-beam elastic body and FBG. Through clever design and fiber layout, they effectively suppressed coupling effects between dimensions. Lai et al. [18] introduced a novel three-axis force sensor for flexible endoscope surgical robots using FBG. The sensor was compared to the commercial Nano17 force sensor, showing measurement errors ranging from 4.50% to 6.18%. Long et al. [19] introduced an ultra-thin triaxial force sensor for the wrist of medical robots based on FBG. The sensor optimized

the traditional cross-beam structure, employed an algorithm to reduce inter-axis coupling, and achieved a maximum sensitivity of 34.07 pm/N. Li et al. [20] designed a 6-DoF F/T tactile sensor with FBG for robot-assisted MIS, featuring nonlinear decoupling, fault tolerance, and temperature compensation. The sensor utilizes a BPNN nonlinear decoupling model, achieving errors within 5% for both I and II types. Layered structures, as a spatially distributed design, have been continuously proposed by researchers for high-performance sensor development in conjunction with FBG. Kim et al. [21] presented a six-axis force sensor for the end effector of minimally invasive surgical robots, incorporating a layered structure and FBG. The sensor exhibited a force resolution of 0.15 N, with a rational FBG parallel layout in the elastic body space. Li et al. [22] developed a six-axis force sensor for orthopedic robots based on a layered structure and FBG. Innovatively integrating a gravity self-compensation method, the sensor achieved dynamic six-axis force measurement with a resolution of 0.0364 mN. Xiong et al. [23] aimed for structural decoupling and proposed a six-axis force/torque sensor for medical robot wrists based on a layered structure and FBG. The resolutions for M_x , M_y , M_z , F_x , F_y , and F_z were $7.8 \text{ N} \cdot \text{mm}$, $7.2 \text{ N} \cdot \text{mm}$, $15.8 \text{ N} \cdot \text{mm}$, 0.0067 N , 0.0066 N , and 0.0825 N , respectively. Guo et al. [24] introduced a 3-D force sensor based on FBG with an internally and externally separated layered structure. The 3-D coupling degrees for F_x , F_y , and F_z were 0.823%, 0.974%, and 0.677%, with sensitivities of 32.567 pm/N, 33.97 pm/N, and 44.116 pm/N, respectively. In these studies, layered structures have been employed to design highly sensitive multidimensional force sensors. However, the aspects of miniaturization and structural self-decoupling have been overlooked. Although separated layered structures offer advantages in miniaturization and structural decoupling to some extent, they encounter challenges such as processing, assembly, and friction.

Addressing the aforementioned challenges, this article is dedicated to developing a high-performance 3-D force sensor specifically designed for medical robotic end-effectors. The sensor adopts a layered measurement strategy, through the introduction of compact elastomers and the integration of five FBGs to achieve miniaturization, structural self-decoupling, and high-sensitivity 3-D force measurement. The application of FBG involves a two-point adhesive packaging method, ensuring the sensor's heightened sensitivity while effectively mitigating the occurrence of chirp effects [25]. Comprehensive theoretical modeling and finite element simulation analyses are conducted to thoroughly investigate the sensor's performance. In-depth studies involving static and dynamic experiments further validate the sensor's capabilities. In addition, medical palpation and acupuncture experiments are performed to affirm the effectiveness of the proposed sensor design.

The rest of this article is organized as follows. Section II introduces the measurement principle, modeling, and simulation of the sensor. Section III describes the static and dynamic experiments of the sensor and the performance comparison with other sensors. Finally, Section IV concludes this article.

TABLE I
TOOL-TISSUE FORCES IN MEDICINE

Items	Measurement range	Resolution
Ablation surgery [26]	0-1.5 N	0.01 N
Acupuncture [27]	$\pm 1.5 \text{ N}$	—
Suture [28]	$\pm 2.5 \text{ N}$	0.01 N
Neurosurgery [29]	<1.86 N	—
Colorectal surgery [30]	1-3 N	—

II. PRINCIPLES AND DESIGN OF SENSORS

A. Sensor Structure

In the medical field, especially in surgical scenarios, physical forces are applied to tissues for contact or resection purposes to achieve therapeutic effects. For a safer and more effective treatment, it is crucial to control the interaction forces between tools and tissues. From Table I demonstrates the range of forces required for common surgeries, such as in cardiac ablation procedures, the force range for tool-tissue contact is between 0 and 1.5 N, with a required resolution of 0.01N [26]. This necessitates that our sensor performance surpasses the operational requirements.

In this article, the sensor is composed of a layered elastic structure, optical fibers, and a protective shell. The exploded schematic diagram of the sensor is shown in Fig. 1(a)-(1). The elastic body comprises a cylindrical helical structure and a hollow cylindrical structure. The helical structure evidences an outstanding capability for axial force transmission, thereby enhancing sensitivity to axial forces (F_z). Simultaneously, the hollow cylindrical body, designed with recesses, is employed for sensitivity to lateral forces (F_x/F_y), with its internal diameter larger than that of the helical structure. Specifically, the hollow cylindrical body is configured with a multilayered groove structure, featuring four elliptical recesses per layer uniformly distributed at 90° intervals. This structural design augments the radial force transmission capability of the sensor. To improve sensor sensitivity and mitigate chirping effects, five FBGs are strategically affixed to the sensor using a two-point bonding approach. Four of these FBGs are uniformly distributed on the outer surface of the elastic body, as shown in Fig. 1(a)-(1), while the fifth FBG is positioned along the central axis of the elastic body. The sensor has layered characteristics and miniaturization (height = 33 mm, diameter = 30 mm), with specific dimensions outlined in Fig. 1(a)-(2).

To ensure the sensor obtains stable strain measurements, pre-stretching of the optical fiber is necessary. We propose a principle for FBG prestretching, which can be described as follows:

$$F_{\text{rm}} S_{\text{des}} \leq D_{\text{pstr}} \leq D_{\text{sd}} \quad (1)$$

where F_{rm} is the maximum value of the measurement range, S_{des} represents sensitive, D_{pstr} is the prestretching amount of the FBG, and D_{sd} is the maximum drift in the FBG's safe range. The sensitivity S_{des} can be obtained from the following:

$$S_{\text{des}} = \frac{1}{R_{\text{des}}} \quad (2)$$

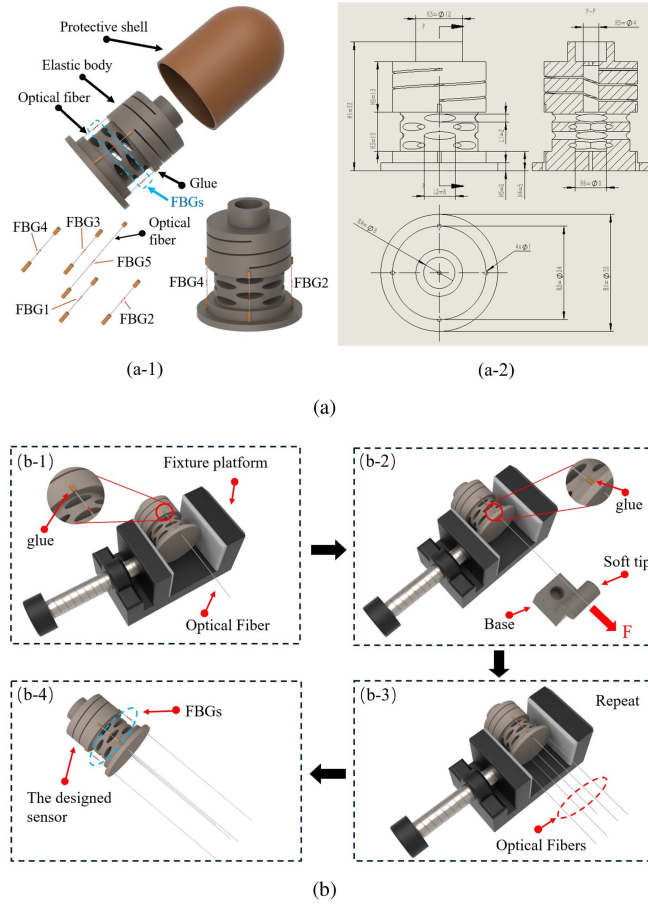


Fig. 1. Sensor system: (a) Sensor structure. (a)-(1) Sensor exploded view and layout of FBGs. (a)-(2) Detailed dimensions of the sensor. (b) Fiber assembly (b)-(1) Fixture clamping sensor bonded fiber end. (b)-(2) Schematic diagram of pre-stretching the fiber. (b)-(3) Completion diagram of fiber bonding. (b)-(4) Final assembly of the sensor.

where R_{des} represents the designed sensor resolution. This value should be greater than or equal to the target resolution R_{goal} , thus

$$R_{\text{des}} \leq R_{\text{goal}}. \quad (3)$$

The range of FBG prestretching can be obtained through (1)–(3). We chose FBGs with a safe drift range within 1500 pm, and the target resolution of the sensor should be better than the common tool-tissue contact force of 0.01 N, as shown in Table I. Through the above formula, we can obtain the range of FBG prestretching as $200 \text{ pm} \leq D_{\text{pstr}} \leq 1500 \text{ pm}$.

By obtaining the range of prestretching, the sensor assembly is carried out as shown in Fig. 1(b). First, the optical fiber is fed into the sensor from the bottom and the distal end of the fiber is pasted into the sensor groove, as shown in Fig. 1(b)-(1). After waiting for the adhesive at the distal end to solidify, the fiber is looped around a base and the fiber drift is adjusted to the prestretching range using standard weights. The proximal end of the fiber is then fixed with adhesive after stretching, as depicted in Fig. 1(b)-(2). This process is repeated for the remaining fibers, as shown in Fig. 1(b)-(3), until all fibers are installed. The final assembled sensor is depicted in Fig. 1(b)-(4).

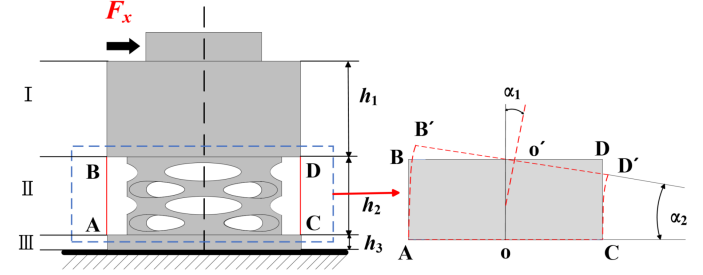


Fig. 2. Mechanical model of the elastic material under the action of F_x . Deformation of FBG 2 and FBG4 under the influence of F_x .

B. Theoretical Modeling of the Elastic Material

In this section, theoretical modeling of the structure will be undertaken. Initially, analysis is conducted on the radial forces acting on the elastic material. Due to the identical strains induced by forces in the x and y directions, emphasis is placed solely on the x -direction loads. Given that the inner diameter of the hollow cylindrical structure is significantly larger than that of the upper helical spring structure, the upper part can be considered a rigid structure. Therefore, stress and deformation analysis can be limited to the hollow cylindrical structure, as shown in Fig. 2. The red lines CD and AB represent the lengths of FBG2 and FBG4, respectively. The elastic body is divided into three parts, labeled I, II, and III, with lengths h_1 , h_2 , and h_3 , respectively. Under the influence of load F_x , optical fibers FBG2 and FBG4 undergo compression and tension, as illustrated in Fig. 2. The total deflection angle of the hollow cylindrical structure is denoted as α_1 . Due to the small deformations involved, the deformation of the hollow cylindrical structure $AB'CD'$ can be approximated as an arc structure, assuming a curvature of $\widehat{AB'} = \widehat{CD'} = \alpha_2$. Based on the geometric deformation of the second section, the following can be derived:

$$\alpha_1 = -\frac{F_x h_1 h_2}{EI_1} - \frac{F_x h_2^2}{2EI_1} = \alpha_2 \quad (4)$$

where E represents the Young's modulus. I_1 is the sectional moment of inertia of the hollow cylinder and can be expressed as $\pi(D^4 - d^4)/64$.

The inner and outer diameters of the hollow cylindrical structure are denoted as d and D , respectively. Assuming a curvature radius of R for the circular arc OO' , the radii corresponding to the circular arc segments AB' and CD' can be derived as $R + D/2$ and $R - D/2$, respectively. Consequently, the average strain $\Delta\varepsilon_{\text{FBG}4}$ of the arc segment AB' can be expressed as

$$\Delta\varepsilon_{\text{FBG}4} = \frac{\widehat{AB'} - \widehat{OO'}}{\sum_{i=1}^3 h_i} = \frac{Dh_2(h_2 + 2h_1)}{4EI_1 \sum_{i=1}^3 h_i} Fx. \quad (5)$$

Similarly, the average strain $\Delta\varepsilon_{\text{FBG}2}$ for the arc segment CD' of the hollow cylinder is described as follows:

$$\Delta\varepsilon_{\text{FBG}2} = -H_1 Fx \quad (6)$$

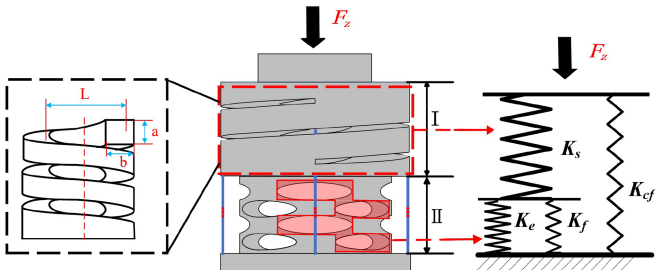


Fig. 3. Mechanical model of the elastic material under the action of F_z .

$$H_1 = \frac{Dh_2(h_2 + 2h_1)}{4EI_1 \sum_{i=1}^3 h_i}. \quad (7)$$

Due to $\Delta\varepsilon_{\text{FBG}2} = -\Delta\varepsilon_{\text{FBG}4}$, it can be inferred that when subjected to the F_x load, the magnitudes of strain generated in FBG2 and FBG4 are equal, but they have opposite directions.

Similarly, under the influence of F_y , the strains generated in FBG 1 and FBG3 are also equal in magnitude but opposite in direction, expressed as

$$\Delta\varepsilon_{\text{FBG}3} = -\Delta\varepsilon_{\text{FBG}1} = H_1 F_y. \quad (8)$$

When the elastic material is subjected to axial force F_z , the primary deformation region is the rectangular cross-section spiral structure, and the hollow cylinder is a secondary deformation area. The strain in FBG5 can be considered as the sum of the deformations in both regions. Therefore, analyzing the effect of axial force on the elastic structure can be simplified as the spring model shown in Fig. 3. The first part represents the rectangular cross-section spiral spring structure, where a and b represent the length and width of the cross-section of the spiral structure, respectively, and L is the diameter of the spiral structure. According to the fundamental formula for spring stiffness, it can be obtained as follows:

$$K = \frac{4GI_\rho}{nL^3\pi} \quad (9)$$

where G represents the shear modulus of the spring material, I_ρ is the polar moment of inertia of the spring section, L is the diameter of the spiral structure, and n is the effective number of spring turns.

From (9), it can be seen that to determine the stiffness of the spring, it is necessary to first calculate its polar moment of inertia. For springs with a rectangular cross-section, the plane assumption is not applicable because the cross-section undergoes torsion during deformation. In such cases, the calculation must rely on the principles of elasticity, and the fundamental formula for this calculation is as follows:

$$I_\rho = \iint_L \left(x^2 + y^2 + x \frac{\partial\varphi}{\partial y} - y \frac{\partial\varphi}{\partial x} \right) dx dy \quad (10)$$

where $\varphi(x, y)$ represents the deformation displacement function of the spring. According to empirical formulas, the torsional displacement function for a rectangular cross-section can be

expressed as

$$\varphi(x, y) = \sum_{m=1}^{\infty} \frac{32a^2(-1)^{\frac{m+1}{2}}}{m^3\pi^3 ch(\frac{mb\pi}{2a})} \sin\left(\frac{m\pi}{2a}x\right) sh\left(\frac{m\pi}{2a}y\right) + xy \quad (11)$$

where $m=1,3,5,\dots$.

Bring (11) into (10) yields

$$\begin{aligned} I_\rho &= \iint_L \sum_{m=1}^{\infty} [2x^2 + R \cdot (x \cdot A - y \cdot B)] dx dy \\ R &= \frac{16a(-1)^{\frac{m+1}{2}}}{m^2\pi^2 ch(\frac{mb\pi}{2a})} \\ A &= \sin\left(\frac{m\pi}{2a}x\right) ch\left(\frac{m\pi}{2a}y\right) \\ B &= \cos\left(\frac{m\pi}{2a}x\right) sh\left(\frac{m\pi}{2a}y\right). \end{aligned} \quad (12)$$

Integrating (12) yields

$$I_\rho = 16a^3b \left[\frac{1}{3} - \frac{64a}{\pi^5 b} \sum_{m=1}^{\infty} \frac{1}{m^5} th\left(\frac{mb\pi}{2a}\right) \right]. \quad (13)$$

Substituting (13) into (9), the stiffness of the rectangular cross-section hollow cylindrical spring can be calculated as

$$K_s = \frac{64Ga^3b}{n\pi L^3} \left[\frac{1}{3} - \frac{64a}{\pi^5 b} \sum_{m=1}^{\infty} \frac{1}{m^5} th\left(\frac{mb\pi}{2a}\right) \right]. \quad (14)$$

In (14), the parameter m is typically chosen to be the first three terms, i.e., $m = 1, 3, 5$. If a more precise spring stiffness is desired, additional terms can be considered for the calculation, the stiffness of the central fiber can be denoted as K_{cf} . Thus, the deformation Δz_1 of the first part of the rectangular cross-section spiral elastic material can be expressed as

$$\Delta z_1 = \frac{F_z}{K_s + K_{cf}}. \quad (15)$$

The second part of the elastic material is a hollow cylindrical body with multiple layers of uniformly shaped and sized elliptical grooves in its midsection. In Fig. 3 area II, the red outlined area represents four elliptical grooves, which are considered as a unit. The entire hollow cylinder can be uniformly divided into four such units. Under the influence of F_z , each unit undergoes the same deformation, and the total force on these four units is equal to F_z . This corresponds to the characteristics of parallel springs. Therefore, the hollow cylinder can be equivalent to four parallel springs, as shown in Fig. 3, each with a stiffness of K_e . The stiffness of the optical fibers distributed on the outer circumferential surface is denoted as K_f . Since the four optical fibers have the same length and are evenly distributed, the total stiffness for Part II is $4K_e + 4K_f$. Thus, Δz_2 represents the axial strain of the hollow cylinder, which can be expressed according to Hooke's Law as

$$\Delta z_2 = \frac{F_z}{4(K_e + K_f)}. \quad (16)$$

The deformation of the elastic material under axial force, denoted as Δz , is obtained from (15) and (16)

$$\Delta z = \Delta z_1 + \Delta z_2 = \left(\frac{1}{K_s + K_{cf}} + \frac{1}{4(K_e + K_f)} \right) F_z. \quad (17)$$

The strain in the axial direction can thus be obtained as $\Delta\varepsilon_{FBG5} = \Delta z$.

Utilizing (6), (8), and (17), the relationship between the central wavelength shift and the applied force and temperature can be obtained

$$\begin{cases} \frac{\Delta\lambda_1}{\lambda_1} = (1 - \rho_e) \Delta\varepsilon_{FBG1} + (\alpha_f + \xi) \Delta T \\ \frac{\Delta\lambda_2}{\lambda_2} = (1 - \rho_e) \Delta\varepsilon_{FBG2} + (\alpha_f + \xi) \Delta T \\ \frac{\Delta\lambda_3}{\lambda_3} = (1 - \rho_e) \Delta\varepsilon_{FBG3} + (\alpha_f + \xi) \Delta T \\ \frac{\Delta\lambda_4}{\lambda_4} = (1 - \rho_e) \Delta\varepsilon_{FBG4} + (\alpha_f + \xi) \Delta T \\ \frac{\Delta\lambda_5}{\lambda_5} = (1 - \rho_e) \Delta\varepsilon_{FBG5} + (\alpha_f + \xi) \Delta T \end{cases} \quad (18)$$

The above equation can be rewritten as

$$\begin{cases} \Delta\lambda_1 = A1\Delta\varepsilon_{FBG1} + B1\Delta T \\ \Delta\lambda_2 = A2\Delta\varepsilon_{FBG2} + B2\Delta T \\ \Delta\lambda_3 = A3\Delta\varepsilon_{FBG3} + B3\Delta T \\ \Delta\lambda_4 = A4\Delta\varepsilon_{FBG4} + B4\Delta T \\ \Delta\lambda_5 = A5\Delta\varepsilon_{FBG5} + B5\Delta T \end{cases} \quad (19)$$

where A is the strain sensitivity coefficient and B is the temperature sensitivity coefficient, there is $A1 = A2 = A3 = A4 = A5$, but B, as the temperature sensitivity coefficient, is usually affected by the encapsulation method and space layout. In the ideal case, when $B1 = B2 = B3 = B4 = B5$ or $\Delta T = 0$, the difference of wavelength drift between FBG4 and FBG2 can be determined by $\Delta\lambda_4 - \Delta\lambda_2$ in relation to the applied force F_x , while eliminating the effect of temperature, and similarly, $\Delta\lambda_3 - \Delta\lambda_1$ can be determined in relation to the wavelength of F_y . And by $\Delta\lambda_3 + \Delta\lambda_1$ can decouple the temperature effect of F_z . Thus, the conversion formula for FBG wavelength drift and force with temperature compensation is realized as

$$\begin{bmatrix} \Delta\lambda_4 - \Delta\lambda_2 \\ \Delta\lambda_3 - \Delta\lambda_1 \\ \Delta\lambda_5 - \frac{1}{2}(\Delta\lambda_1 + \Delta\lambda_3) \end{bmatrix} = \lambda_0(1 - \rho_e) \begin{bmatrix} C_1 \end{bmatrix}_{3 \times 3} \begin{bmatrix} F_x \\ F_y \\ F_z \end{bmatrix}. \quad (20)$$

where $[C_1]_{3 \times 3}$ can be expressed as

$$\begin{bmatrix} C_1 \end{bmatrix}_{3 \times 3} = \begin{bmatrix} 2H_1 & 0 & 0 \\ 0 & 2H_1 & 0 \\ 0 & 0 & H_2 \end{bmatrix} \quad (21)$$

where $H_2 = 1/(K_s - K_{cf})$

When the temperature sensitivity coefficients of the optical fiber are unequal, specifically with $B1 \neq B2 \neq B3 \neq B4 \neq B5$ and $\Delta T \neq 0$, there is the following relationship:

$$B4 = Q_1 B2 \quad (22)$$

$$B3 = Q_2 B1 \quad (23)$$

$$B5 = \frac{Q_3}{2}(B1 + B3) \quad (24)$$

TABLE II
SENSOR SIMULATION PARAMETERS

Component	Flexure	Optical fiber	Glue
Material	Photosensitive resin	Silica	Epoxy resin
Young's modulus(GPa)	3	72	3.3
Density(kg/m ³)	1120	2500	1180
Poisson ratio	0.44	0.17	0.35

where Q1, Q2, and Q3 are temperature scaling coefficients, which need to be obtained by temperature experiments. At this point, the experiment has a temperature-compensated FBG wavelength drift and force conversion formula as follows:

$$\begin{bmatrix} \Delta\lambda_4 - Q_1\Delta\lambda_2 \\ \Delta\lambda_3 - Q_2\Delta\lambda_1 \\ \Delta\lambda_5 - \frac{Q_3}{2}(\Delta\lambda_1 + \Delta\lambda_3) \end{bmatrix} = \lambda_0(1 - \rho_e) \begin{bmatrix} C_2 \end{bmatrix}_{3 \times 3} \begin{bmatrix} F_x \\ F_y \\ F_z \end{bmatrix} \quad (25)$$

where $[C_2]_{3 \times 3}$ can be expressed as

$$\begin{bmatrix} C_2 \end{bmatrix}_{3 \times 3} = \begin{bmatrix} (1 + Q_1)H_1 & 0 & 0 \\ 0 & (1 + Q_2)H_1 & 0 \\ 0 & 0 & H_3 \end{bmatrix} \quad (26)$$

where $H_3 = H_2 + (1 - Q_3)\Delta z_2$

The two matrices obtained are suitable for temperature compensation in stable and varying temperature environments, respectively.

C. Performance Study and Simulation Based on FEM

To verify the static characteristics of the sensor, numerical simulation was performed using ANSYS. Given that the elastic body serves as the primary sensing component, the analysis focused exclusively on the elastic body. In order to facilitate low-cost and rapid prototype validation, photosensitive resin (Resin model: Future 4600; Manufacturer: Future Factory, Shenzhen, China.) was employed in this study to prepare the elastic body for 3-D printing. The simulation parameters for the sensor material are outlined in Table II. During the simulation, fixation was applied to the lower surface of the elastic body, and loading was exerted on the cylindrical component at the top of the elastic body.

The elastic strain performance of the sensor was analyzed using Ansys as shown in Fig. 4(a) when the elastic body is subjected to a load from the x-direction, FBG1 and FBG3 experience equal but opposite tensile and compressive strains. Therefore, the wavelength difference of FBG1 and FBG3 represents F_x . Similarly, the wavelength difference of FBG2 and FBG4 represents F_y . The central fiber FBG5 represents F_z . The simulated load range for lateral force is -2 N to 2 N, and for axial force, it is 0 to 2.5 N. Fig. 4(b)-(d) displays the deformation and strain results of the sensor under different loads, with colors indicating the bending information of the sensor under the load. It can be observed that there is a linear correlation between fiber strain and the corresponding force.

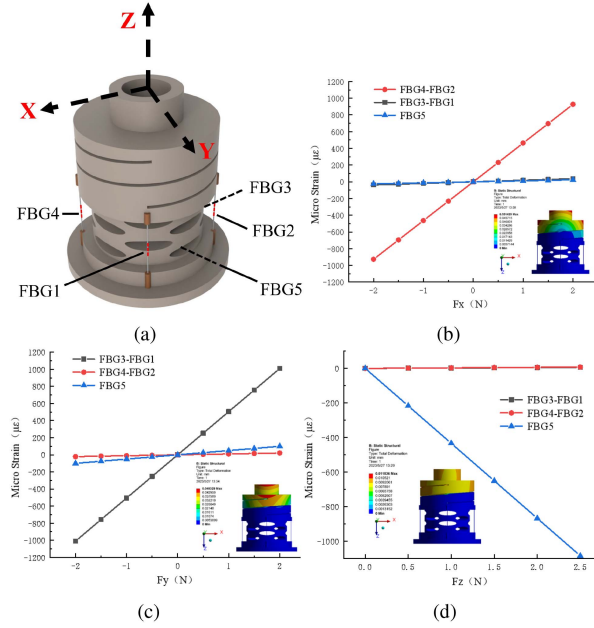


Fig. 4. Simulation of the relationship between FBG and applied force.

The dynamic characteristics play a crucial role in determining the application range of sensors. In this article, utilizing Solidworks simulation, model analysis of the first five natural frequencies and modes was conducted. The analysis results show that the first mode corresponds to the vibration in the X direction and dominates the response, with a natural frequency of 605.46 Hz. According to practical engineering experience, it is common to define the working range of the sensor as two-thirds of the first natural frequency, i.e., 0–403.6 Hz.

D. Multiobjective Optimization

With the increasing variety of materials available for sensor manufacturing, it becomes crucial to design sensors that can adapt to different material applications while maintaining similar performance. Different materials lead to varying structural dimensions. To validate the applicability of the proposed structure, here we select five key parameters of the sensor structure as the optimization variables: p_1, p_2, p_3, p_4 , and p_5 represent the inner diameters of the second and first parts of the sensor, respectively, the width and height of the elliptical slot, and the height of the spiral groove. Two types of materials, metallic aluminum and nonmetallic polyetheretherketone (PEEK), are chosen as the subjects of optimization. It is worth mentioning that PEEK material has excellent biocompatibility and has been successfully applied in the medical field [31]. The selected parameters $P = \{p_1, p_2, p_3, \dots\}$, with the constraint conditions set as follows:

$$\begin{cases} l_{1\min} < p_1 < l_{1\max} \\ l_{2\min} < p_2 < l_{2\max} \\ l_{3\min} < p_3 < l_{3\max} \\ l_{4\min} < p_4 < l_{4\max} \\ l_{5\min} < p_5 < l_{5\max} \\ \varepsilon_{\min} < \varepsilon < \varepsilon_{\max} \end{cases} \quad (27)$$

TABLE III
PERFORMANCE PARAMETER TABLE OF THE SENSOR

Force	FBG	Sensitivity (pm/N)	R-square (%)	Linearity (%)	Hysteresis (%F.S.)
F_x	FBG2	94.87	0.9922	3.37	2.7
	FBG4	81.21	0.9965	2.75	
F_y	FBG1	98.35	0.9965	4.11	3
	FBG3	103.52	0.9726	6.03	
F_z	FBG5	102.48	0.9993	2.48	5

The finite element software Workbench is used to solve the problem, and a sensitivity analysis of the parameters is conducted. By employing the response surface methodology to analyze key parameters, the relationship between constraints and the objective function is obtained, as shown in Fig. 5(c), which allows for the derivation of two structures with similar performance characteristics, as shown in Fig. 5(d). The results indicate that structures with similar capabilities in different materials can be achieved through a multiobjective optimization approach.

III. EXPERIMENTS AND STRUCTURE

A. Calibration Experiments

In order to establish the relationship between the strain and load on the sensor, a static calibration system was constructed in this study, as shown in Fig. 6(a). The system consists of a calibration platform, FBG interrogator (frequency 100 Hz, resolution 1 pm), PC, sensor base, adjustable bracket, loading cap, and weight. As shown in Fig. 6(b), a loading device was designed with the sensor fixed on the calibration platform and a loading cap installed on top. Standard weights were connected to the loading cap via a thin rope and supported using pulleys. The five FBGs of the sensor were connected to the interrogator, and the wavelength signals were sent to the computer for analysis and processing.

In the calibration experiments, the calibration ranges for radial force and axial force on the sensor were $[-4, 4]$ N and $[0, 5]$ N, respectively. Loading and unloading were performed with increments of 0.5 N in each dimension, and each set of calibrations is repeated six times. The relationship between the center wavelength shift of FBGs and external force was determined using the average wavelength shift. The calibration results are shown in Fig. 7(a), (c), (e), and Table III, revealing a strong linear relationship between the wavelength shift of each FBG and the corresponding applied load, with R-squared values very close to 1. The maximum sensitivities for FBG1, FBG2, FBG3, FBG4, and FBG5 were 98.35 pm/N, 94.87 pm/N, 103.52 pm/N, 81.21 pm/N, and 102.48 pm/N, respectively. In Fig. 7(b), (d), and (f), the blue, green, and red surfaces represent the relationships between strain and F_x , F_y , and F_z , respectively. It can be observed that the interaxis coupling is minimal when subjected to applied loads, with the minimum coupling errors in the three directions being 0.38%F.S(F_x - F_z), 0.01%F.S(F_y - F_z), and 0.6%F.S(F_z - F_x), respectively. It is noteworthy that the current structure is fabricated using 3-D printing, and if metal processing

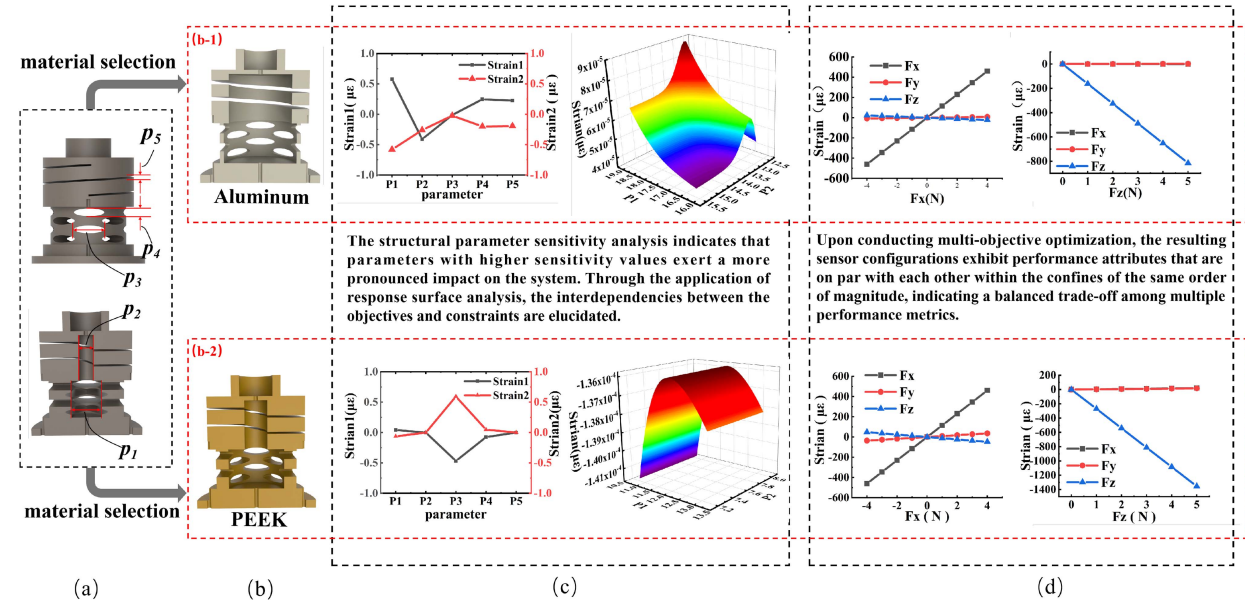


Fig. 5. Multiobjective optimization process for aluminum and PEEK materials: (a) Cross-section of the original structure. (b) Cross-section of the structures for aluminum and PEEK materials after optimization. (c) Optimization process. (d) Performance after optimization.

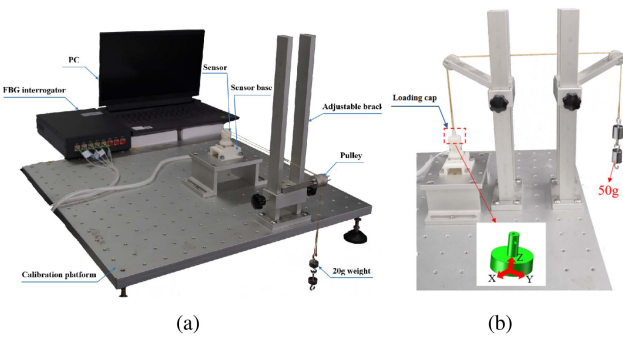


Fig. 6. Calibration system. (a) Sensor calibration platform. (b) Axial force calibration method.

is employed, its performance is expected to be further enhanced. This indicates that our sensor's structure is capable of achieving self-decoupling.

Through static standard experiments, we can obtain the sensitivity matrix $[C_1]_{3 \times 3}$ as

$$[C_1]_{3 \times 3} = \begin{bmatrix} 178.93 & 0 & 0 \\ 0 & 201.86 & 0 \\ 0 & 0 & 93.34 \end{bmatrix}. \quad (28)$$

B. Creep Experiment and TC Experiment

1) *Creep Experiment*: Creep characteristics are one of the important performance parameters of the sensor, and the quality of creep performance affects the measurement accuracy. Doctor palpation typically takes a few minutes to obtain an initial assessment, while the needle insertion process in acupuncture therapy may only take a few seconds. Therefore, in the creep experiment, a random direction 1 N constant load was applied to the sensor for 20 min. The experimental results are shown in

Fig. 8(b), with average errors of 2.09%, 0.86%, and 1.26% for the three directions, respectively.

2) *Temperature compensation Experiment*: The temperature experiment system is shown in Fig. 9(a). The test temperature range was from 25 °C to 40 °C, with temperature intervals of 5 °C. The experimental results are shown in Fig. 9(b), with the temperature sensitivity coefficients for FBG1 to FBG5 being 8.14 pm/°C, 17.66 pm/°C, 15.6 pm/°C, 11.9 pm/°C, and 13.98 pm/°C, respectively. In this experiment, we used the same type of FBG, however, the different temperature sensitivity coefficients of these FBGs are related to the temperature compensation, which is influenced by the temperature change rate and the encapsulation of the optical fiber [32]. In this study, the FBGs were fixed with glue manually applied, making it difficult to control the thickness of the glue, resulting in inconsistent sensitivity. Therefore, from Fig. 9(b), we obtained the temperature scaling factors Q_1 and Q_2 for the x and y directions as 0.674 and 1.9, respectively. For the z direction, the temperature compensation was performed using the sum of FBG1 and FBG3, as indicated in Fig. 9(c), showing a temperature curve sensitivity of 23.74 pm/°C, resulting in a temperature scaling factor Q_3 of 0.589.

The sensitivity matrix obtained through static calibration and temperature experiments is as follows:

$$[C_2]_{3 \times 3} = \begin{bmatrix} 149.76 & 0 & 0 \\ 0 & 292.7 & 0 \\ 0 & 0 & 99.79 \end{bmatrix}. \quad (29)$$

3) *Real-Time Temperature Compensation Experiment*: We established an experimental system as shown in Fig. 9(d)-(1), mainly consisting of a heating platform, sensor, interrogator, and computer. The experimental procedure was as follows: the heating platform simulated the heat source in actual applications, placed in the direction of force applied to the sensor. The temperature was first raised from room temperature to 40 °C, then increased in increments of 20 °C up to 100 °C, while a

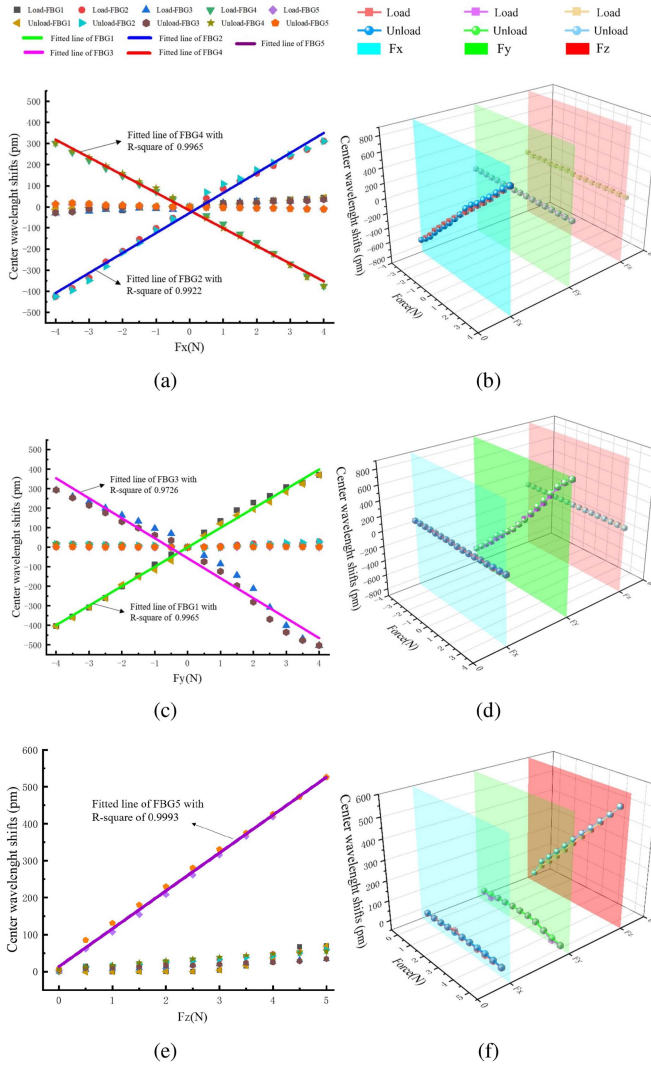


Fig. 7. (a), (c), and (e) represent the scattering diagrams of the wavelength change of five optical fibers under the influence of force, respectively. (b), (d), and (f) represent the relationship between load (F_x , F_y , and F_z) and wavelength shift, respectively.

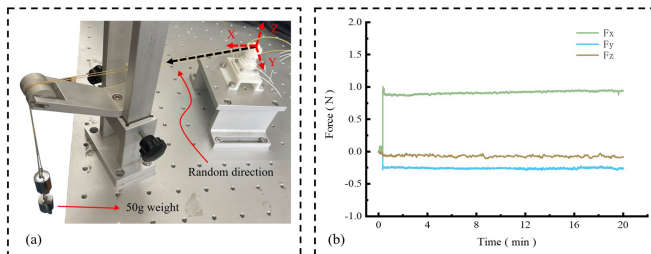


Fig. 8. Creep resistance experiment and corresponding results. (a) Loading method for the experiment. (b) Outputs in three directions.

constant force of 1 N was applied to the sensor. The purple line represents no temperature compensation, while the black line represents temperature compensation. The experimental results indicate that the output is closer to the true value after temperature compensation. The average error between the sensor's temperature compensation and the loading is 1.75%.

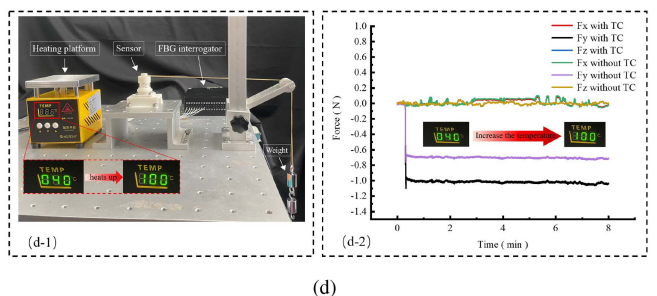
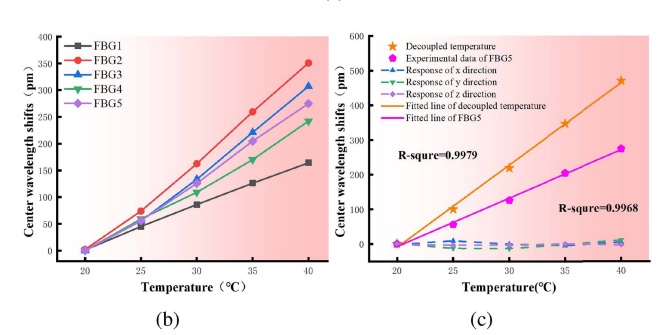
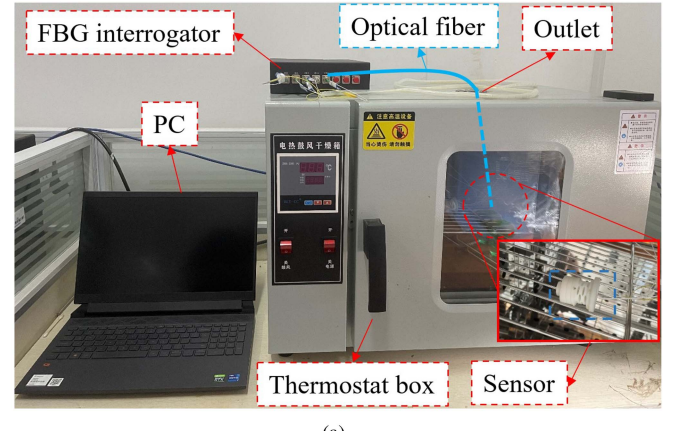


Fig. 9. (a) Temperature compensation experimental setup. (b) The curve of optical fiber under temperature variations. (c) Fitted line of the temperature response and temperature interference curves for the three force components. (d)-(1) Dynamic performance experiment setup. (d)-(2) The output curves of the dynamic temperature experiment.

C. Dynamic Performance Experiment

1) Dynamic Performance Comparison: To verify the dynamic loading performance of the designed sensor, a dynamic comparison system was constructed, as illustrated in Fig. 10(a). The sensor developed in this study was secured on the desktop, while a commercial force sensor (ATI Nano17) was fixed on a micromanipulator platform. The comparison of tracking performance between the proposed sensor and the commercial sensor in all three directions is shown in Fig. 10(b). The minimum tracking error is 3.89% F.S.

2) Dynamic Force Perceptive Experiment: To investigate the dynamic force sensing performance of the sensor, we designed an experiment as shown in Fig. 11(a), where the sensor was subjected to a constant load. Subsequently, The hairline abruptly severed around 21 sec, with the output value plummeting to a minimum of -94.5 mN, then it returned to the range of

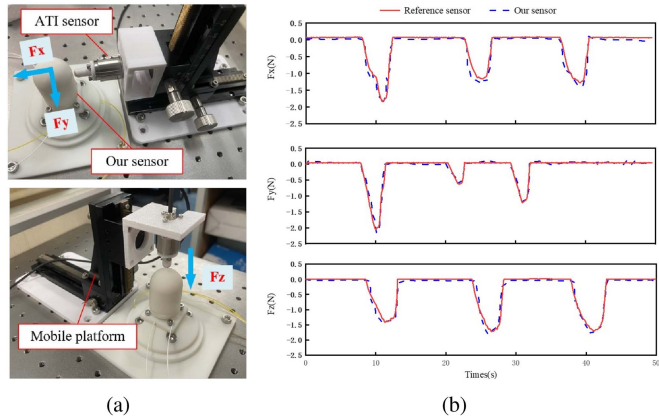


Fig. 10. Calibration System: (a) The sensor proposed in this paper does dynamic force tracking with ATI Nano17. (b) Dynamic tracking effect with ATI Nano17.

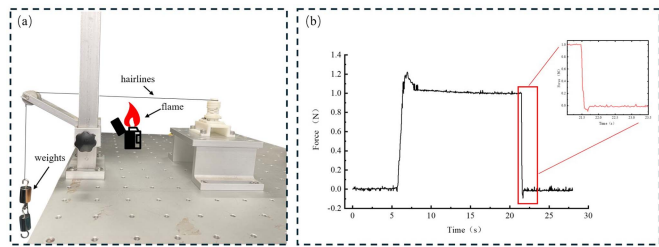


Fig. 11. (a) Experimental setup. (b) Experimental output curve.

± 0.02 N within approximately 50 ms. The response curve exhibited stability as depicted in Fig. 11(b).

D. Cooperate With the Robot for Medical Operation

Palpation is a crucial clinical diagnostic technique, with the physician applying pressure to the patient's body surface to examine abnormal conditions such as lumps or nodules in local tissues. As shown in Fig. 12(a), a sphere with a radius of 4 mm was utilized in this study to simulate pathological nodules.

The sensor is precisely adapted to the terminus of the robotic arm, concurrently establishing 9 contact points on a pig liver. The robot engages in contact with a horizontal motion increment of 10 mm and a downward compression depth of 4 mm, repeating this process twice. The force distribution cloud map of the Fz during the measurement process is depicted in Fig. 12(b), where conspicuous peaks in the contact force Fz are evident at locations with nodular masses. The 3-D force data during the palpation process is presented in Fig. 12(c). Experimental validation attests to the remarkable performance of the sensor in palpation experiments, demonstrating its effective measurement of the interactive force information between the robot and organ tissues.

To deeply investigate the force-sensing performance of sensors in more intricate operations, a system mimicking human acupuncture capabilities has been constructed, as depicted in Fig. 13(a). Comprising a mechanical arm, a screw-driven sliding platform, a newly proposed sensor, a needle inserter, and simulated skin, the system integrates various components. The

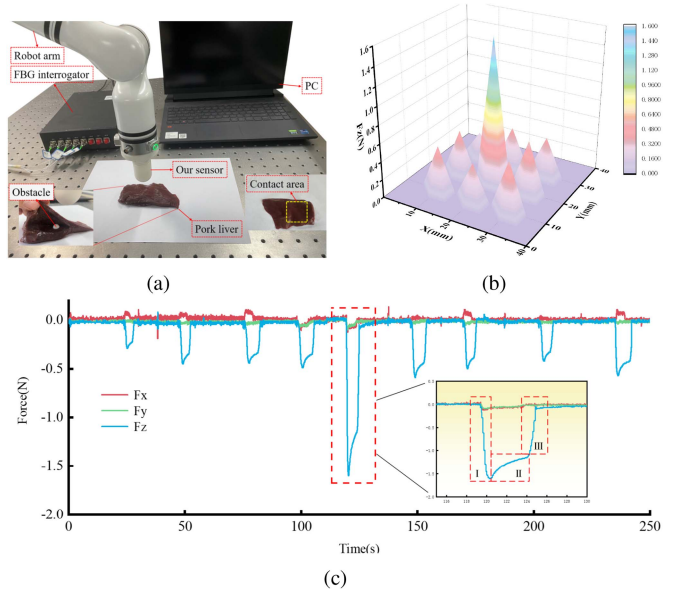


Fig. 12. (a) Tactile examination experimental setup. (b) Force distribution at different sensor contact points. (c) Ex vivo experiment evaluation results.

acupuncture process can be divided into four stages: the first stage involves piercing the surface of the skin, the second stage entails traversing the first layer of skin tissue into the second layer, the third stage involves piercing the deepest layer of skin and maintaining position, and the fourth stage involves withdrawing from the second layer.

The system underwent 3-D force measurements during both vertical insertion and random angle insertion modes, as depicted in Fig. 13(b) and (c). Two needle penetration experiments were conducted for each insertion mode, revealing similar trends in the penetration curves. In needle penetration experiments, the sensor effectively reflects the hardness of different tissue types in both the simulated skin model and the puncture process. The similarity in trend between the two sets of experimental results confirms the stability and effectiveness of the designed sensor in acupuncture experiments, providing valuable insights for acupuncture research.

E. Performance Comparison of Force Sensor

To better describe the characteristics of the proposed sensor, a comparison was made with conventional needle-type and touch sensors. As shown in Table IV, the resolution of some sensors goes as low as 1.5 mN, or even 0.93 mN [33], [34], [35], [36]. Still, they can only detect one-dimensional force information, thereby limiting their applicability. Other sensors can capture information in higher dimensions, but their resolution exceeds 20 mN [34], [35], making it challenging to detect subtle force changes. In contrast, the sensor proposed in this study can simultaneously measure 3-D forces ($F_z = \pm 5$ N, $F_{xy} = \pm 4$ N), maintaining a small resolution of 5 mN, exhibiting excellent detection performance in palpation and needle penetration experiments. It should be noted that the simulation range of the proposed sensor is smaller than the experimental range. This

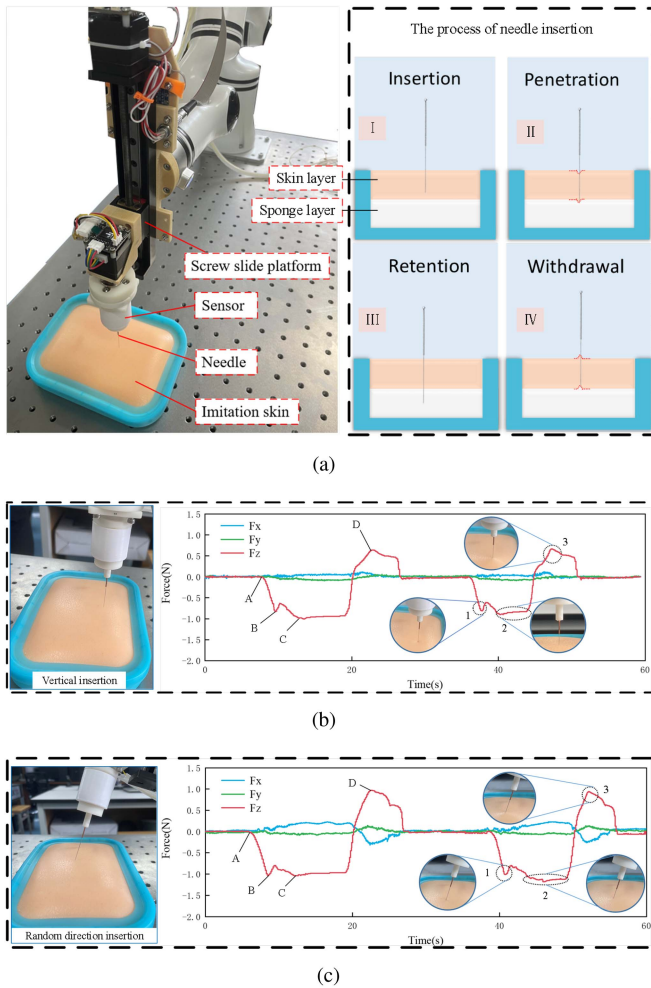


Fig. 13. (a) Tactile examination experimental setup and the acupuncture process. (c) and (d) Underwent three-dimensional force measurements during vertical and random angle insertion modes.

TABLE IV
PERFORMANCE COMPARISON OF SENSORS BASED ON DIFFERENT METHODS

Group	Range (N/N-mm)	Res (mN/N-mm)	DOF	Application
Li et al [33]	Fz=5	Fz=0.93	1	Tissue Palpation
Xiong et al [34]	Fz=5	Fz=30	2	Needle Insertion
Puangmali et al [35]	Mz=10	Mz=0.8		
	Fxy=± 1.5	F=20	3	Tissue Palpation
Shi et al [36]	Fz=6	Fz=1.5	1	Needle Insertion
Our	Fxy=±4	Fxy=5.6;5	3	Needle Insertion
	Fz=±5	Fz=9.8		Tissue Palpation

difference arises from inconsistencies between simulation parameters and actual material parameters, as well as simplifications made in the simulation model. In addition, manufacturing and assembly errors are factors that cannot be overlooked. Sensitivity differences between optical fibers are caused by manual assembly, leading to inconsistent pretensioning between fibers.

IV. CONCLUSION

Based on a layered structure, a high-performance FBG 3-D force sensor was designed for medical robot end-effectors with self-decoupling capabilities. The sensor is miniaturized (height = 33 mm, diameter = 30 mm). The first layer of the elastic body employs a helical structure to measure axial forces, while the second layer uses a slotted hollow cylindrical structure for radial force sensing. The sensor's performance was evaluated through static calibration and dynamic force loading experiments. Operating within a frequency range of 0–403.6 Hz, the sensor achieved impressive results. In the lateral force measurement range of ± 4 N for F_x and F_y , the sensor demonstrated resolutions of 5.59 mN and 4.95 mN, respectively. For axial force F_z within a measurement range of ±5 N, the resolution was 9.75 mN. The sensor reached a maximum sensitivity of 201.86 pm/N. Regarding cross-talk errors, the sensor displayed minimal interference in the three directions, with values of 0.38% F.S (F_x - F_z), 0.01% F.S (F_y - F_z), and 0.6% F.S (F_z - F_x). The sensor's exceptional resolution and accuracy were verified through in vitro organ experiments and needle insertion tasks.

For future work, we plan to manufacture the elastic body using metal to reduce hysteresis and the sensor's size, thereby achieving lightweight and compact design, and expanding the range of applications for the force sensor.

REFERENCES

- [1] P. E. Dupont et al., "A decade retrospective of medical robotics research from 2010 to 2020," *Sci. Robot.*, vol. 6, no. 60, 2021, Art. no. eabi8017.
- [2] J. H. Li, C. Y. Wang, Z. Y. Mao, Y. Liu, Z. D. Wang, and H. Liu, "A compact FBG-based triaxial force sensor with parallel helical beams for robotic-assisted surgery," *IEEE Trans. Instrum. Meas.*, vol. 71, 2022, Art. no. 7503709.
- [3] T. L. Li, A. Q. Pan, and H. L. Ren, "A high-resolution triaxial catheter tip force sensor with miniature flexure and suspended optical fibers," *IEEE Trans. Ind. Electron.*, vol. 67, no. 6, pp. 5101–5111, Jun. 2020.
- [4] Q. Liang, J. Long, G. Coppola, D. Zhang, and W. Sun, "Novel decoupling algorithm based on parallel voltage extreme learning machine (PV-ELM) for six-axis F/M sensors," *Robot. Comput.-Integr. Manuf.*, vol. 57, pp. 303–314, 2019.
- [5] A. Song, J. Wu, G. Qin, and W. Huang, "A novel self-decoupled four degree-of-freedom wrist force/torque sensor," *Measurement*, vol. 40, no. 9/10, pp. 883–891, 2007.
- [6] Q. Liang, D. Zhang, Q. Song, Y. Ge, H. Cao, and Y. Ge, "Design and fabrication of a six-dimensional wrist force/torque sensor based on e-type membranes compared to cross beams," *Measurement*, vol. 43, no. 10, pp. 1702–1719, 2010.
- [7] Y. R. Lee, J. Neubauer, K. J. Kim, and Y. Cha, "Multidirectional cylindrical piezoelectric force sensor: Design and experimental validation," *Sensors*, vol. 20, no. 17, 2020, Art. no. 4840.
- [8] I. Payo, J. M. Adánez, D. R. Rosa, R. Fernandez, and A. S. Vázquez, "Six-axis column-type force and moment sensor for robotic applications," *IEEE Sens. J.*, vol. 18, no. 17, pp. 6996–7004, Sep. 2018.
- [9] R. Shu, Z. G. Chu, H. C. Jiao, and H. Y. Shu, "Contact force sensing of l-shaped structure for robotic end-effectors," *IEEE-ASME Trans. Mechatron.*, vol. 29, no. 1, pp. 455–465, Feb. 2024.
- [10] Q. Liang, D. Zhang, Y. Wang, and Y. Ge, "Development of a touch probe based on five-dimensional force/torque transducer for coordinate measuring machine (CMM)," *Robot. Comput.-Integr. Manuf.*, vol. 28, no. 2, pp. 238–244, 2012.
- [11] L. Fu, A. Song, and D. Chen, "A polyetheretherketone six-axis force/torque sensor," *IEEE Access*, vol. 7, pp. 105391–105401, 2019.
- [12] Z. He and T. Liu, "Isotropy optimization of six-axis capacitive force sensor with a large moment-to-force ratio," *IEEE Trans. Instrum. Meas.*, vol. 71, 2022, Art. no. 7506011.
- [13] A. R. Ahmad, T. Wynn, and C. Y. Lin, "A comprehensive design of six-axis force/moment sensor," *Sensors*, vol. 21, no. 13, 2021, Art. no. 4498.

- [14] Q. Liang et al., "Multi-component FBG-based force sensing systems by comparison with other sensing technologies: A review," *IEEE Sens. J.*, vol. 18, no. 18, pp. 7345–7357, Sep. 2018.
- [15] Q. K. Liang et al., "A force/position measurement method of surgical forceps based on fiber Bragg gratings," *IEEE Sens. J.*, vol. 23, no. 1, pp. 363–373, Jan. 2023.
- [16] D. W. Lai, Z. X. Tang, J. C. Zhao, S. X. Wang, and C. Y. Shi, "Design and validation of a miniature fiber Bragg grating-enabled high-sensitivity torque sensor," *IEEE Sens. J.*, vol. 21, no. 18, pp. 20027–20035, Sep. 2021.
- [17] L. Xiong, G. Jiang, Y. Guo, and H. Liu, "A three-dimensional fiber Bragg grating force sensor for robot," *IEEE Sens. J.*, vol. 18, no. 9, pp. 3632–3639, May 2018.
- [18] W. Lai, L. Cao, J. Liu, S. C. Tjin, and S. J. Phee, "A three-axial force sensor based on fiber Bragg gratings for surgical robots," *IEEE-ASME Trans. Mechatron.*, vol. 27, no. 2, pp. 777–789, Apr. 2021.
- [19] J. Long, Q. Liang, W. Sun, Y. Wang, and D. Zhang, "Ultrathin three-axis FBG wrist force sensor for collaborative robots," *IEEE Trans. Instrum. Meas.*, vol. 70, 2021, Art. no. 3519115.
- [20] T. Li, J. Guo, H. Zheng, S. Wang, L. Qiu, and H. Ren, "Fault-tolerant six-axis FBG force/moment sensing for robotic interventions," *IEEE-ASME Trans. Mechatron.*, vol. 28, no. 6, pp. 3537–3550, Dec. 2023.
- [21] C. Kim and C.-H. Lee, "Development of a 6-DoF FBG force–moment sensor for a haptic interface with minimally invasive robotic surgery," *J. Mech. Sci. Technol.*, vol. 30, pp. 3705–3712, 2016.
- [22] T. L. Li, F. Y. Chen, Z. B. Zhao, Q. F. Pei, Y. G. Tan, and Z. D. Zhou, "Hybrid data-driven optimization design of a layered six-dimensional FBG forcemoment sensor with gravity self-compensation for orthopedic surgery robot," *IEEE Trans. Ind. Electron.*, vol. 70, no. 8, pp. 8568–8579, Aug. 2023.
- [23] L. Xiong, Y. X. Guo, G. Z. Jiang, X. L. Zhou, L. Jiang, and H. H. Liu, "Six-dimensional force/torque sensor based on fiber Bragg gratings with low coupling," *IEEE Trans. Ind. Electron.*, vol. 68, no. 5, pp. 4079–4089, May 2021.
- [24] Y. Guo, J. Kong, H. Liu, H. Xiong, G. Li, and L. Qin, "A three-axis force fingertip sensor based on fiber Bragg grating," *Sens. Actuator A-Phys.*, vol. 249, pp. 141–148, 2016.
- [25] T. L. Li, C. Y. Shi, and H. L. Ren, "Three-dimensional catheter distal force sensing for cardiac ablation based on fiber Bragg grating," *IEEE-ASME Trans. Mechatron.*, vol. 23, no. 5, pp. 2316–2327, Oct. 2018.
- [26] P. Polygerinos, L. D. Seneviratne, R. Razavi, T. Schaeffter, and K. Althoefer, "Triaxial catheter-tip force sensor for MRI-guided cardiac procedures," *IEEE-ASME Trans. Mechatron.*, vol. 18, no. 1, pp. 386–396, Feb. 2013.
- [27] J. Xu and A. Song, "A miniature multiaxis force/torque sensor for acupuncture," *IEEE Sens. J.*, vol. 23, no. 7, pp. 6660–6671, Apr. 2023.
- [28] J. Peirs et al., "A micro optical force sensor for force feedback during minimally invasive robotic surgery," *Sens. Actuator A-Phys.*, vol. 115, no. 2/3, pp. 447–455, 2004.
- [29] A. K. Golahmadi, D. Z. Khan, G. P. Mylonas, and H. J. Marcus, "Tool-tissue forces in surgery: A systematic review," *Ann. Med. Surg.*, vol. 65, 2021, Art. no. 102268.
- [30] S. F. Hardon, R. J. V. Kasteren, J. Dankelman, H. J. Bonjer, and T. Horeman, "The value of force and torque measurements in transanal total mesorectal excision (tatme)," *Technol. Coloproctol.*, vol. 23, no. 9, pp. 843–852, 2019.
- [31] S. Verma, N. Sharma, S. Kango, and S. Sharma, "Developments of peek (polyetheretherketone) as a biomedical material: A focused review," *Eur. Polym. J.*, 2021, Art. no. 110295.
- [32] L. Xiong, G. Z. Jiang, Y. X. Guo, Y. Kuang, and H. H. Liu, "Investigation of the temperature compensation of FBGs encapsulated with different methods and subjected to different temperature change rates," *J. Lightw. Technol.*, vol. 37, no. 3, pp. 917–926, Feb. 2019.
- [33] T. L. Li, C. Y. Shi, and H. L. Ren, "A high-sensitivity tactile sensor array based on fiber Bragg grating sensing for tissue palpation in minimally invasive surgery," *IEEE-ASME Trans. Mechatron.*, vol. 23, no. 5, pp. 2306–2315, Oct. 2018.
- [34] P. Xiong, X. Huang, Y. Li, and P. X. Liu, "A fiber Bragg grating sensing structure for the design, simulation and stress strain monitoring of human puncture surgery," *Sensors*, vol. 19, no. 14, 2019, Art. no. 3066.
- [35] P. Puangmali, H. B. Liu, L. D. Seneviratne, P. Dasgupta, and K. Althoefer, "Miniature 3-axis distal force sensor for minimally invasive surgical palpation," *IEEE-ASME Trans. Mechatron.*, vol. 17, no. 4, pp. 646–656, Aug. 2012.
- [36] C. Y. Shi, Z. X. Tang, and S. X. Wang, "Design and experimental validation of a fiber Bragg grating-enabled force sensor with an ortho-planar spring-based flexure for surgical needle insertion," *IEEE Trans. Med. Robot. Bionics*, vol. 3, no. 2, pp. 362–371, May 2021.



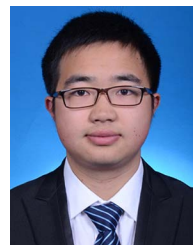
Qiaokang Liang (Senior Member, IEEE) received the Ph.D. degree in control science and engineering from the University of Science and Technology of China, Hefei, China, in 2011.

He is currently a Professor with the College of Electrical and Information Engineering, Hunan University, Changsha, China, where he is also the Vice Director of the National Engineering Research Center of Robot Vision Perception and Control. His research interests include robotic perceptions, advanced robot technology, and application of artificial intelligence technology in perceptions.



Songtao Ouyang received the B.S. degree in mechanical design, manufacturing and automation from Hunan International Economics University, Changsha, China, in 2020. He is currently working toward the Ph.D. degree in control science and engineering with Hunan University, Changsha, China.

His research interests include optical fiber sensing technology for medical and industrial robots



Jianyong Long (Member, IEEE) received the M.S. degree in agricultural informatization from Northeast Forestry University, Harbin, China, in 2017, and the Ph.D. degree in control science and engineering from Hunan University, Changsha, China, in 2022.

He works as an Associate Researcher with Hunan University, China, and his main research interests are in machine learning, robotics, and mechatronics.



Li Zhou received the B.S. degree in automation, in 2019, from East China University of Technology, Nanchang, China, where he is currently working toward the M.S. degree with the College of Electrical and Information Engineering, Hunan University, Changsha, China.

His research interests include machine vision and robotics systems.



Dan Zhang (Senior Member, IEEE) received the Ph.D. degree in mechanical engineering from Laval University, Quebec City, QC, Canada, in June 2000.

He is a Chair Professor of intelligent robotics and automation with The Hong Kong Polytechnic University, Hong Kong. His research interests include robotics and mechatronics, high-performance parallel robotic machine development, micromanipulation/ nanomanipulation and MEMS devices, and rehabilitation robots and rescue robots.

Dr. Zhang is a fellow of the Canadian Academy of Engineering (CAE), the Engineering Institute of Canada (EIC), the American Society of Mechanical Engineers (ASME), and the Canadian Society for Mechanical Engineering (CSME), and a Senior Member of SME